Modification of the spectroscopic properties of Tb_2O_3 phosphor under the high-pressure phase transitions sequence

M. T. Candela,[a,c] F. Aguado,* [b,c] J. González-Lavín,[a] J. A. González[b,c] and R. Valiente[a,c]

[a.] Applied Physics Department. University of Cantabria. Avda. Los Castros 48, 39005- Santander. Spain

[b.] CITIMAC Department. University of Cantabria. Avda. Los Castros 48, 39005- Santander. Spain

[c.] Nanomedicine Group. IDIVAL. Avda. Cardenal Herrera Oria, 39011- Santander. Spain

Abstract

The high-pressure behavior of cubic Tb_2O_3 phase (C-type) has been investigated by *in situ* photoluminescence and Raman spectroscopy up to 18 GPa and 22 GPa, respectively. The luminescence spectrum of Tb_2O_3 at ambient conditions shows its characteristic sharp-line emission bands with the most intense one corresponding to the $^5D_4$ - $^7F_5$ transition, responsible of the green emission. Excitation and emission spectra measured at low temperature and at different emission and excitation wavelengths suggest that photoluminescence is governed by the Tb^{3+} in the non-centrosymmetric site (C_2). A phase transition between 7.2 and 8.6 GPa is observed by Raman and photoluminescence experiments and is associated to a cubic-to-monoclinic (B-type) structural transformation. From 14 GPa the predominant modes in the Raman spectrum correspond to those from the trigonal phase (A-type), indicating that the pressure-induced structural phase transition sequence of Tb_2O_3 is C $\rightarrow$ B $\rightarrow$ A. Upon pressure release, the starting cubic phase is not recovered, but the monoclinic one.

Keywords: phosphors, high-pressure, phase transitions, luminescence, inelastic light scattering

* Corresponding author: aguadof@unican.es

1. Introduction

Rare earth sesquioxides (RE_2O_3) have attracted much interest in the last decades due to their unique physical and chemical properties [1],[2] and the wide range of applications that can show.[3],[4],[5],[6] RE_2O_3 exhibit polymorphism and mainly exist in three structural conformations, commonly named as A-, B- and C-types, corresponding to trigonal (*P-3m1* space group), monoclinic (*C2/m* space group) and cubic (*Ia-3* space group) symmetry, respectively.[1] At ambient conditions, the stable phase depends on the ionic radii of the RE cation. Thus, RE_2O_3 with larger ionic radii (RE= La-Nd) normally crystallize in A-type structure, while those with smaller size (Tb-Lu and Y, Sc) adopt the C-type structure. Moreover, RE_2O_3 composed of medium size cations (RE=Sm-Gd) can be found forming B-type or C-type structures, depending on their synthesis procedure and thermal history.[7]

The density of RE_2O_3 polymorphs is $\rho_A > \rho_B > \rho_C$ at ambient conditions, so with increasing pressure, where volume is decreased, it is expected the phase transition sequence to be C $\rightarrow$ B $\rightarrow$ A in RE sesquioxides.[8] There is still some controversy though, since direct C $\rightarrow$ A transformation has also been reported for several RE_2O_3, such as Gd_2O_3, Eu_2O_3 or Sm_2O_3. [8],[9],[10],[11]. Also, particle size (*bulk*/nano) could play a role in the structural behavior of these compounds under pressure, including changes in both the phase sequence and the transition pressure, as it happens in Er_2O_3, where the transition pressure is increased when working at the nanoscale.[12]

Optical, chemical and electronic properties of RE_2O_3 are derived from their characteristic 4*f* electronic shells.[13] The luminescence spectra of pure or RE^{3+}-

doped sesquioxides, consist of sharp lines whose positions are not strongly affected by the crystallographic environment (although their intensities and splittings do). They are due to electric and magnetic dipole transitions involving *f-f* transitions.[14] Among RE_2O_3 compounds, systems based on Eu_2O_3, Tb_2O_3 or Yb_2O_3 have attracted much attention because of the green (Tb^{3+}), red (Eu^{3+}) or infrared (Yb^{3+}) luminescence in the pure compounds. Usually a non-luminescent oxide host lattice, doped with a luminescent RE is used instead for luminescent applications, in order to avoid luminescence quenching at high RE concentration. Additionally, luminescence from RE^{3+} can be used as a local probe to track phase transitions under pressure or temperature, since their intensities and crystal-field splittings are sensitive to changes of the crystal environment.

Tb_2O_3 crystallizes in the cubic bixbyite-type structure (C-type) with sixteen formula units per unit cell (Z = 16), [15] where the 32 Tb^{3+} cations, which are surrounded by oxygen anions in six-fold coordination and forming distorted octahedrons, are distributed on sites with C_2 symmetry (24) and C_{3i} symmetry (8). Terbium oxides comprise not only the terbium sesquioxide Tb_2O_3, but also the stoichiometric oxide TbO_2 (CaF_2-type structure) and non-stoichiometric oxides such as Tb_4O_7, $Tb_{12}O_7$, $Tb_{11}O_{20}$, Tb_6O_{11} or $Tb_{16}O_{30}$, which are mixed-valence (III, IV) Tb compounds. [16] The presence of Tb^{4+} ions in Tb_2O_3 compound can be considered a drawback regarding its luminescent properties, as they act as luminescence quenching centers of the Tb^{3+} luminescence and facilitate non-radiative processes, decreasing the total luminescence efficiency. [17]

In this paper we report the spectroscopic characterization of the C-type Tb_2O_3 phase at low temperatures and under high-pressure conditions by means of Raman and photoluminescence (PL) techniques. Raman and the Tb^{3+}

photoluminescence measurements evidence a C $\rightarrow$ B $\rightarrow$ A phase sequence in the 0-22 GPa range.

2. Materials and Methods

2.1 Materials and synthesis procedures

Commercial samples of Tb_2O_3 (99.99%, Sigma Aldrich) were used without further purification. Isostructural Tb-doped Y_2O_3 (0.2 mol% or 40 mol%) nanoparticles were synthesized for comparison with pure Tb_2O_3. The nanocrystals were prepared by a solvothermal procedure [18], which can be described as follows: $Y(NO_3)_3 \cdot 6H_2O$ (2.518 mmol) and $Tb(NO_3)_3 \cdot 6H_2O$ (0.005 mmol) are dissolved in a mixture of ethylenglycol and deionized water (30 ml, 19:1). The solution is heated up while stirring until the nitrates are dissolved and subsequently introduced in a stainless-steel autoclave, which is heated at 180ºC for 24h. After the autoclave was naturally cooled to room temperature, the obtained solid was washed and centrifuged with EtOH:H_2O (1:1)(1x100 ml) and deionized water (3x100 ml). The solid is then dried at 70ºC and calcined in air at 1000ºC for 4h. The calcination of the Y_2O_3: Tb (40 mol%) sample at 1000ºC produced the partial oxidation of Tb^{3+} to Tb^{4+}. Already at 800ºC the presence of Tb^{4+} is visible to the naked eye by the brown color of the nanocrystals.

2.2 Characterization

X-ray diffraction (XRD) experiments were performed in a Bruker D8 Advanced diffractometer equipped with a Cu tube ($\lambda_{K\alpha 1,2}$=1.5418 Å) and a Lynxeye 1-D detector. XRD patterns were recorded in the 10º-110º (2θ) range with a 0.03º step. Rietveld method performed with TOPAS software was used for phase

checking and structural refinement. Reflectance measurements were taken in a Cary 6000i spectrophotometer, capable of measuring in the UV-visible-NIR spectral range from 175 nm to 1800 nm with a resolution of 0.01 nm, using an integrating sphere. Photoluminescence, excitation and lifetime measurements as a function of temperature (300-10 K) were performed using a FLSP920 spectrofluorometer (Edinburg instruments) equipped with a continuous 450 W and a 4 W supercontinuum from Fianium for excitation, double monochromators and an electrically cooled Hamamatsu R928P photomultiplier tube (PMT) as a detection system. Raman experiments as a function of temperature as well as at high pressure were carried out with a T64000 Raman spectrometer (Horiba), equipped with a nitrogen cooled CCD as a detector, which is coupled to a confocal microscopy, using the 514.5 nm line of a Kr^+-Ar^+–laser. Photoluminescence measurements at high pressure were performed using this device with the 488 nm line. For high pressure experiments, samples were loaded in a Boehler-Almax or a membrane diamond anvil cells (DAC), using paraffin oil as a pressure transmitting medium and ruby microspheres for pressure calibration, through the R-line pressure dependence. For low temperature experiments, a MicrostatHe (Oxford instruments) or a closed cycled cryostat (ARS) were used.

3. Results and discussion

3.1 Characterization at ambient conditions and at low temperature

Powder X-Ray diffraction (XRD) measurements were taken to check the crystal structure and phase purity of terbium oxide. From the Rietveld analysis (Fig. 1(a)), it is found that the phase of Tb_2O_3 at ambient conditions is C-type with

lattice parameter *a* =10.7293(1) Å, and no distinguishable traces of other terbium oxides were detected within the experimental uncertainty. Fig. 1(b) shows the reflectance spectrum of Tb_2O_3 compared with the one of Y_2O_3:Tb (40 mol%), which contains Tb^{3+} and Tb^{4+} ions.

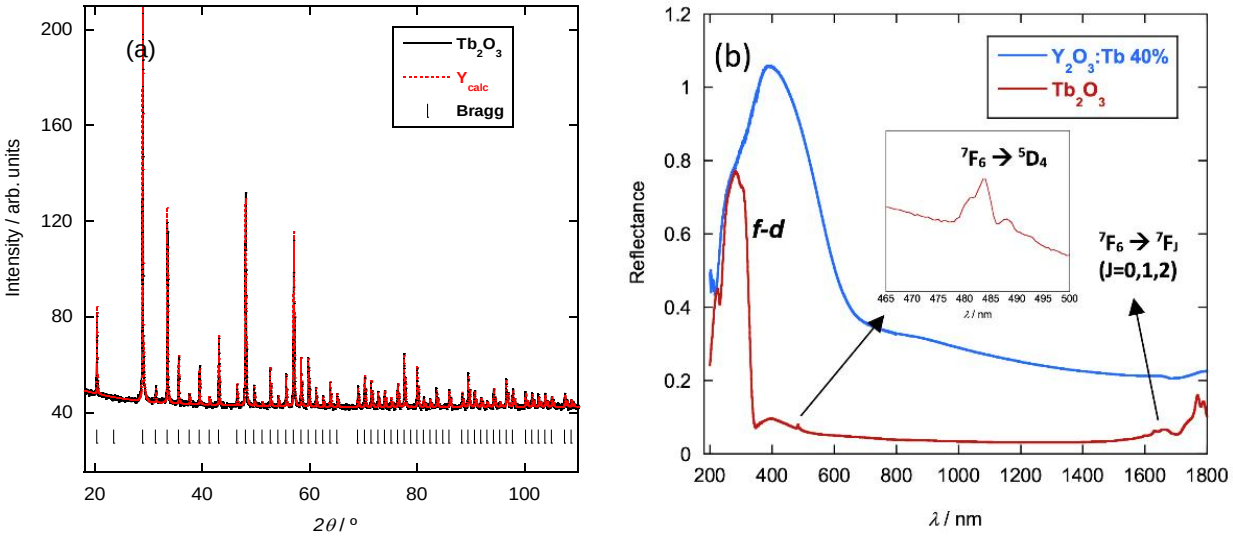

Fig. 1. (a) Refined X-ray powder diffraction pattern of Tb_2O_3 at ambient conditions. The indexed Bragg peaks for the cubic phase are shown. (b) Reflectance spectra of Tb_2O_3 powder and Y_2O_3:Tb (40 mol%) with Tb^{3+} and Tb^{4+} ions. The one of Y_2O_3:Tb has been shifted in the y-axis for clarity reasons.

Several features can be observed in the reflectance spectrum of Tb_2O_3: 1) a broad absorption band below 345 nm , 2) absorption peaks located at 483.7 nm and from 1460 nm to the end of the spectra, corresponding to forced electric dipole 4*f*-4*f* transitions of the Tb^{3+} cations with C_2 symmetry,[19] 3) a low reflectance plateau from 550 to 1380 nm. On the other hand, the reflectance spectrum of Y_2O_3:Tb (40 mol%) is dominated by a band centered at 390 nm due to Tb^{4+} ions induced after thermal treatment (see Experimental section).

It is worth mentioning that if the sample had small traces of Tb^{4+} it would acquire a slight brownish-color and the sample under study (Tb_2O_3) was pristine white,

indicating that only Tb^{3+} is present, as corroborated by the XRD measurements and the absent of remarkable absorption peaks in the visible spectral range.

Raman spectroscopy provides useful information about polymorphism, chemical composition and lattice dynamics. In Tb_2O_3, as in other C-type sesquioxides, the irreps that represent their optic and acoustic modes are: $\Gamma = 4A_g + 4E_g + 14T_g + 5A_{2u} + 5E_u + 17T_u$, where A_g, E_g and T_g are Raman active modes, A_u and E_u are silent modes, sixteen T_u correspond to infrared active modes and one T_u is related to acoustic vibrations. Therefore, up to 22 modes are expected in the Raman spectra, although in general the number of observed experimental Raman peaks is smaller. Fig. 2 shows a comparation of the Tb_2O_3 Raman spectra at 9 K, 124 K and room temperature. The Raman modes were assigned based on the experimental and theoretical study of this compound by Ibáñez *et al.* [20] In our sample, only 9 of the 22 Raman active modes are clearly visible in the spectra at ambient conditions.

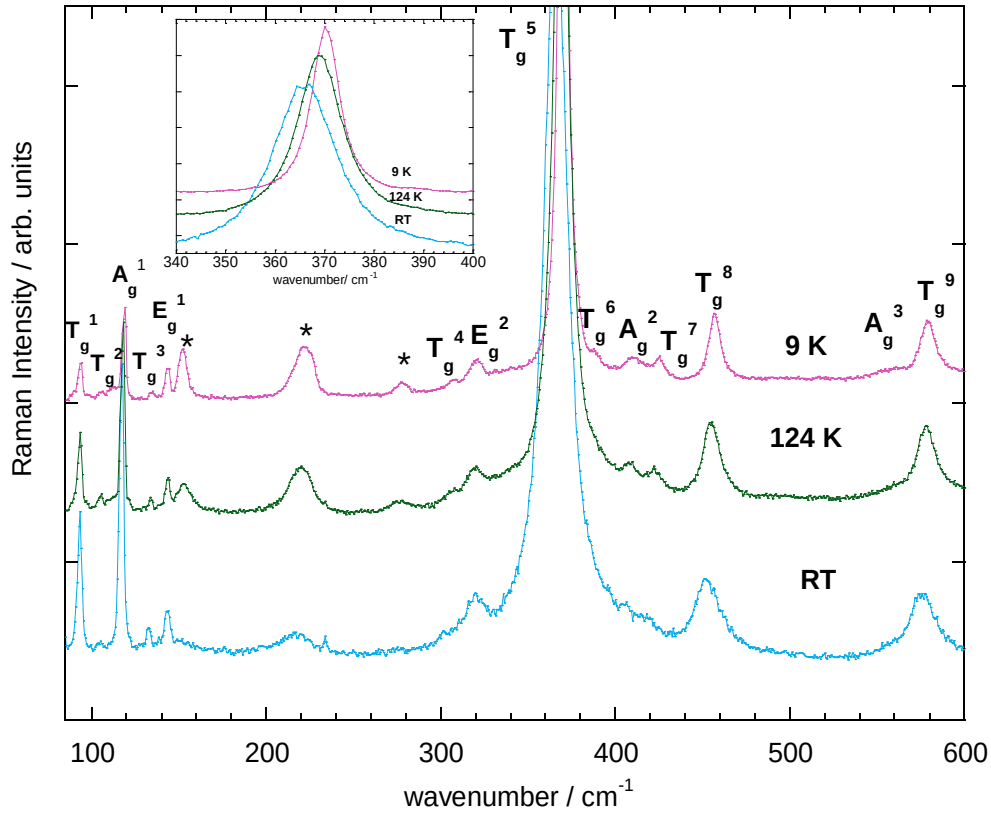

Fig. 2. Raman spectra of Tb_2O_3 for selected temperatures. Peaks with an asterisk have been tentatively assigned to local vibrational modes, as in ref [20].

Table 1 shows the assignment of the experimental Raman active modes of Tb_2O_3 with their corresponding energy and width (FWHM) at 9 K and 300 K. The most intense peak, which is located at 366 cm^{-1}, corresponds to a T_g mode (T_g^5 in Table 1, hereafter C-T_g peak), although in other C-type RE_2O_3 compounds, a combination of T_g+ A_g modes are reported.[21],[22]

Table 1. Assignment, frequency, and full width at half maximum (FWHM) of the Tb_2O_3 Raman active modes at 9 K and RT.

Symmetry	9K		RT	
	ω(cm^{-1})	FWHM(cm^{-1})	ω (cm^{-1})	FWHM(cm^{-1})
T_g^1	93.4(1)	2.6(3)	93.0(1)	2.4(1)
T_g^2	105.4(6)	3(1)	104.9(6)	3(1)
A_g^1	118.5(1)	2.2(1)	117.1(1)	2.1(1)
T_g^3	134.7(3)	2(1)	132.5(3)	1.8(8)
E_g^1	143.3(1)	2.3(7)	143.2(2)	3.8(6)
T_g^4	306.7(7)	4(2)	-	-
E_g^2	319.7(3)	5.6(8)	318.9(4)	7(1)
T_g^5	370.2(1)	6.8(3)	365.9(2)	14.9(6)
T_g^6	387(1)	-	-	-
A_g^2	411.2(5)	5(1)	-	-
T_g^7	424.8(3)	4.3(9)	-	-
T_g^8	456.9(1)	6.8(3)	451.3(3)	15(1)
A_g^3	558(1)	8(4)	-	-
T_g^9	579.0(2)	10.2(4)	576.0(3)	18.1(9)

Given the considerable intensity of this peak, it will be used as a local probe to study possible temperature or pressure-induced phase variations. The temperature behavior of the Tb_2O_3 Raman modes has been investigated in the 9-300 K range. At 9K, some peaks that are not clearly visible at room temperature, mainly the weakest features around the C-T_g peak, become well defined allowing us to distinguish up to 14 Raman modes. At this temperature also appear some bands (marked with asterisks in the spectra) that are reported to be local vibrational rather than Raman modes. [20] The C-T_g, T_g^8 and T_g^9 peaks shift noticeably towards lower frequencies when increasing temperature while the rest of the peaks, do not change their position significantly. The peak widths also increase upon rising temperature, as it is shown in the inset of Fig. 2 for the C-T_g mode. The variation of the frequency $\omega(T)$ of the Raman modes as a function of temperature can be modelled by the formula proposed by Balkanski *et al.* [23] (Eq. 1), where the temperature dependence arises from the decay of an optical phonon into two or three acoustic phonons with the same energies, derived from the cubic and quartic anharmonic contributions in the vibrational potential energy

$$\omega(T) = \omega_0 + A[1 + 2n(\omega_0/2, T)] + B[1 + 3n(\omega_0/3, T) + 3n(\omega_0/3, T)^2] \quad (1)$$

where $n(\omega, T) = 1/(e^x - 1)$ and $x = \hbar\omega/(k_B T)$. The dependence of the peak width (FWHM) with temperature $\Gamma(T)$ can be described through Eq. 2. [24]

$$\Gamma(T) = \Gamma_0 + \Gamma^{EPC}(T) + \Gamma^{an}(T) \quad (2)$$

where the term Γ_0 is temperature-independent and stands for the width contribution due to the finite spectrometer resolution and other scattering mechanisms (defects, impurities), Γ^{EPC} represents the contribution from the electron-phonon coupling and Γ^{an} denotes the anharmonic phonon-phonon interactions. The terms Γ^{EPC} and Γ^{an} can be modelled by equations (3) and (4)

$$\Gamma^{EPC}(T) = \Gamma^{EPC}(0)[n(-\omega_0/2, T) - n(\omega_0/2, T)] \qquad (3)$$

$$\Gamma(T) = C[1 + 2\, n(\omega_0/2, T)] + D[1 + 3n(\omega_0/3, T) + 3n(\omega_0/3, T)^2] \quad (4)$$

In all equations ω_0 represent the zone-center phonon energy at 0 K, k_B is the Boltzmann constant, T the absolute temperature and A, B, C and D are fitting parameters representing the anharmonic constants. Fig. 3 shows the temperature dependence of the Raman frequency shift and *FWHM* for the C-T_g mode of Tb_2O_3.

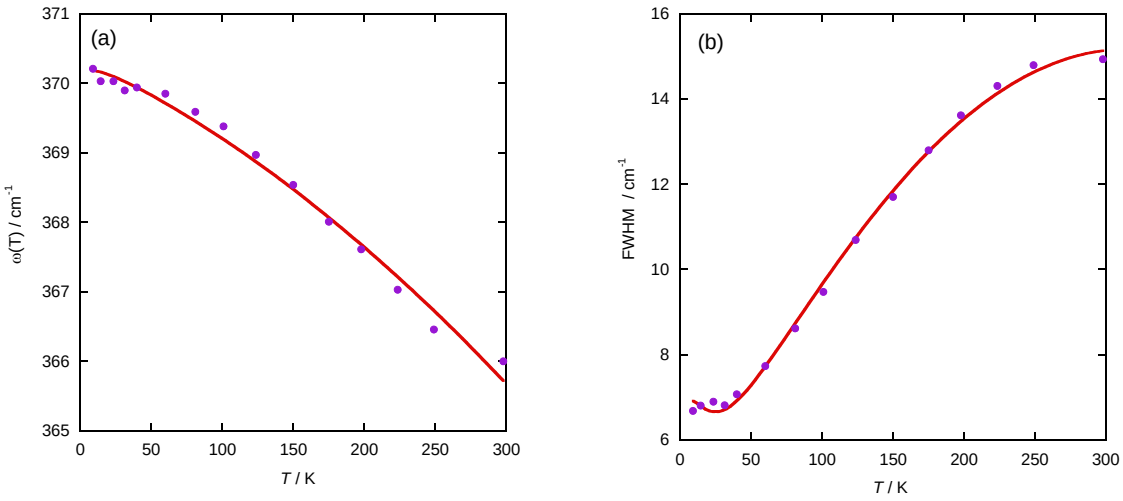

Fig. 3. Temperature dependence of the Raman frequency (a) and peakwidth for the C-T_g mode of Tb_2O_3 (b).

From Fig. 3 we can observe that equations (1) and (2) provide a good fit of the peakwidth (*FWHM*) and Raman frequency temperature behavior and allow us to extrapolate the peakwidth and Raman frequency at 0 K (ω_0). The fitting parameters are given in Table 2. As it can be observed from Table 2, the anharmonic constants *A* and *C* are several times larger than *B* and *D* constants, suggesting that it is much more probable the process in which an optical phonon decay into two acoustic phonons, rather than three. Similar behavior in the ratio of the anharmonic constants *A*/*B* has been observed in other compounds such as Ho_2O_3, [25] Lu_2O_3,[26] $ReSe_2$ and $SnSe_2$. [27]

The phonon lifetime τ can be calculated through the Raman spectrum by the relation shown in eq. (5):

$$\frac{1}{\tau} = \frac{\Delta E}{\hbar} = 2\pi c\Gamma \qquad (5)$$

where ΔE is the uncertainty in the energy of the phonon mode and c is the speed of light (in cm/s). Fig 4 shows the phonon lifetime temperature dependence of the Tb_2O_3 C-T_g Raman mode. The phonon lifetimes have been calculated using the value of the FWHM obtained at each temperature after subtracting the obtained instrumental contribution, Γ_0 (Table 2).The lifetime of the phonon decreases as temperature increases (as it is inversely proportional to the FWHM) and reaches its maximum value τ = 1.57 ps at 9 K.

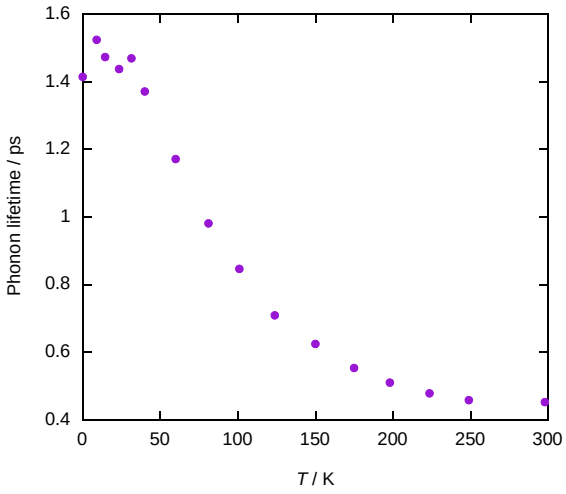

Fig. 4. Phonon lifetime temperature dependence for the C-T_g Raman mode of Tb_2O_3.

Fig. 5 shows the RT and 10 K excitation (a) and luminescence (b) spectra of Tb_2O_3. The emission spectra recorded at RT under 323 nm excitation consist of sharp-line emission bands from $^5D_4$ excited state to low lying multiplets ^7F_J (J = 0-6), with the most intense peak located at 541 nm (543 nm at 10 K) corresponding to the $^5D_4$ - $^7F_5$ transition, which is the main responsible for the terbium green emission. There is no evidence of emission from $^5D_3$ level. This can be due to terbium-terbium interactions, which are very probable owing to the high concentration of Tb^{3+} leading to cross-relaxation mechanisms involving the process ($^5D_3 \rightarrow {}^5D_4$) + ($^7F_6 \rightarrow {}^7F_1$, $^7F_2$), that increase the $^5D_4$

population multiplet at the expense of the $^5D_3$ one. [28] The excitation spectra recording Tb^{3+} emission at 550 nm consist of two groups of narrow peaks, centered at about 375 nm and 483 nm, that corresponds to transitions from the $^7F_6$ ground state to $^5D_4$ and $^5D_3$ excited states of Tb^{3+}. The broad intense bands below 330 nm, also observed in the reflectance spectrum, are assigned to 4f-5d interconfigurational transitions. [29], [30]

The comparison of the RT absorption (Fig. 1b) and excitation spectrum (Fig. 5a) seems to point out that the band at around 400 nm in Fig.1b could be attributed to undesired traces of Tb^{4+}.

Table 2. Best fit values for the parameters refined during the fitting process of the Raman frequency and peakwidth temperature dependence of the C-T_g Tb_2O_3 mode.

ω_0 (cm^{-1})	$\Gamma(T=0K)$ (cm^{-1})	Γ_0 (cm^{-1})	$\Gamma^{EPC}(0)$ (cm^{-1})	A (cm^{-1})	B (cm^{-1})	C (cm^{-1})	D (cm^{-1})
370.4(1)	7(1)	3.2(5)	2.1(4)	-0.21(4)	-0.005(2)	1.7(1)	-0.034(3)

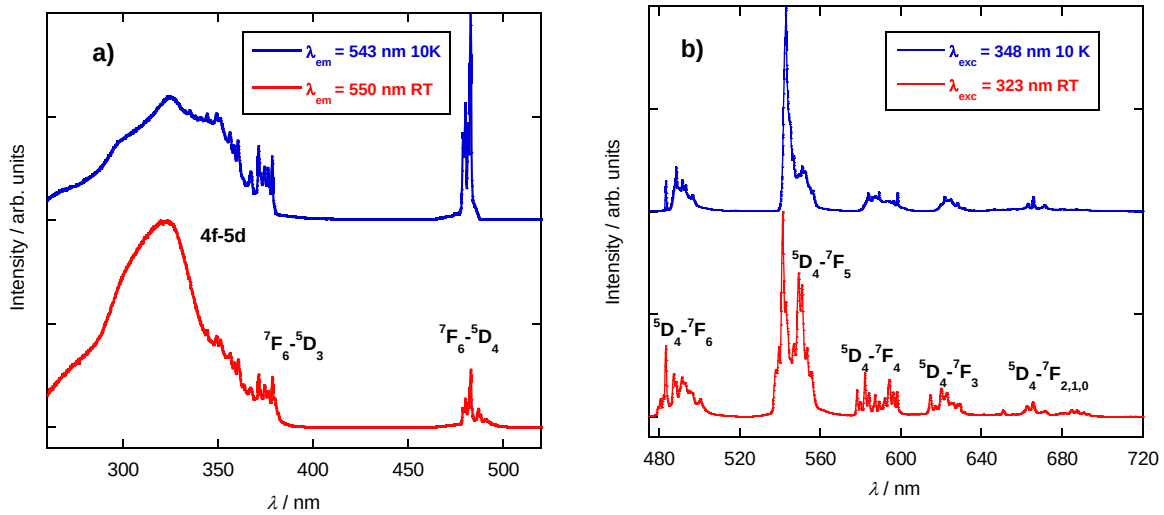

Fig. 5. 10 K and RT Excitation (a) and emission (b) spectra of Tb_2O_3. Excitation and detection wavelengths are indicated.

Emission and excitation spectra of Tb_2O_3 were also measured at low temperatures. As previously stated, in the C-type structure of Tb_2O_3 there are two different sites for Tb^{3+} cations, which have C_2 and C_{3i} symmetry in a ratio 3:1, where the abundant site is the one with C_2 symmetry. In the isostructural Y_2O_3 doped with 0.2% Tb^{3+}, both sites have been clearly identified (Fig. 6(a)), which is in agreement with what has been reported in the literature for that compound doped with different amount of Tb^{3+} ions. [31],[32] However, this is not the case of the pure Tb_2O_3 compound, where the RT emission spectrum (in green, Fig. 6(a)) is identical to that assigned to C_2 site by fluorescence lifetimes. The C_2 present higher oscillator strength than the C_{3i} and therefore shorter lifetime. We can deduce that we are observing just one Tb^{3+} crystallographic site (C_2), which is non-centrosymmetric and the most abundant. The ratio between the integrated intensity of the magnetic transition $^5D_4 \rightarrow {}^7F_6$, which is less sensitive to the coordination environment, and the one of the electric dipole transition $^5D_4 \rightarrow {}^7F_5$ (also referred as the hypersensitive transition), is found to be 0.21 for Tb^{3+} in S_6 site of Y_2O_3 and 0.35 for both, Tb^{3+} in C_2 site of Y_2O_3 and in Tb_2O_3.

The temporal evolution of the $^5D_4$ to $^7F_5$ Tb^{3+} luminescence has been obtained from 9 K to RT, detecting at 543 nm after short pulsed excitation at 482 nm. The decay curves have been fitted with a bi-exponential function and an average lifetime has been calculated using eq. (6).

$$< \tau > = \frac{A_1\tau_1^2 + A_2\tau_2^2}{A_1\tau_1 + A_2\tau_2} \qquad (6)$$

where A_1 and A_2 are the pre-exponential factors and τ_1 and τ_2 are the decay time of each exponential. The average fluorescence lifetime is found to range from hundreds of microsecond (0.35 ms) at 10 K to nanosecond (1.6 ns) at RT. The

temperature dependence of the average lifetime (Fig. 6b) can be described with an Arrhenius-type equation (inset Fig 6b), where E_a is the activation energy, k_B is the Boltzmann constant, τ_{rad} is a temperature independent rate constant and τ_0 is a frequency factor for the thermally assisted de-activation process. From this model, an activation energy of E_a = 7.9 meV (63.9 cm^{-1}) is obtained and the temperature at which lifetime drops to half its maximum value is found to be 17 K. The short PL lifetime (ns), bright green emission and its density makes Tb_2O_3 a good candidate for scintillation applications.

3.2 Characterization at high pressure

In order to study the high-pressure structural evolution of polycrystalline Tb_2O_3, Raman experiments were performed for pressures up to 22 GPa in a Boehler-Almax DAC, using the ruby R-line luminescence scale for pressure estimation. Fig. 7 (a) shows representative Raman spectra. The Raman modes shift towards higher frequencies with increasing pressure, indicating contraction of the Tb-O bonding, although this is less noticeable for the low frequency modes (Fig 7(b)). At 7.45 GPa, there is a decrease in the relative intensity of the Raman peaks, especially visible for the peaks located at 396 cm^{-1} (C-T_g) and 123 cm^{-1}, when compared with those at ambient pressure. The T_g mode located around 490 cm^{-1} broadens and a new contribution starts to appear by its side, indicating the development of a new crystalline phase. At 8.2 GPa, there is an intensity inversion for the lowest frequency Raman peaks (80-123 cm^{-1}) and the new contribution, although not well-defined, is evident. At 9.8 GPa, the C-T_g peak drops in intensity and the new contribution splits into two peaks. Also, at this pressure, a new set of broad bands became visible in the 140-380 cm^{-1} range,

being then up to 13 Raman modes visible in the spectra. Now, the most intense peak at 114 cm^{-1} has growth in intensity at the expense of its nearest peaks, that appears just as a shoulder in the spectra. According to group theory, there are predicted up to 21 Raman modes for B-type structure ($14A_g + 7B_g$ modes), and up to 4 Raman active modes for A-type

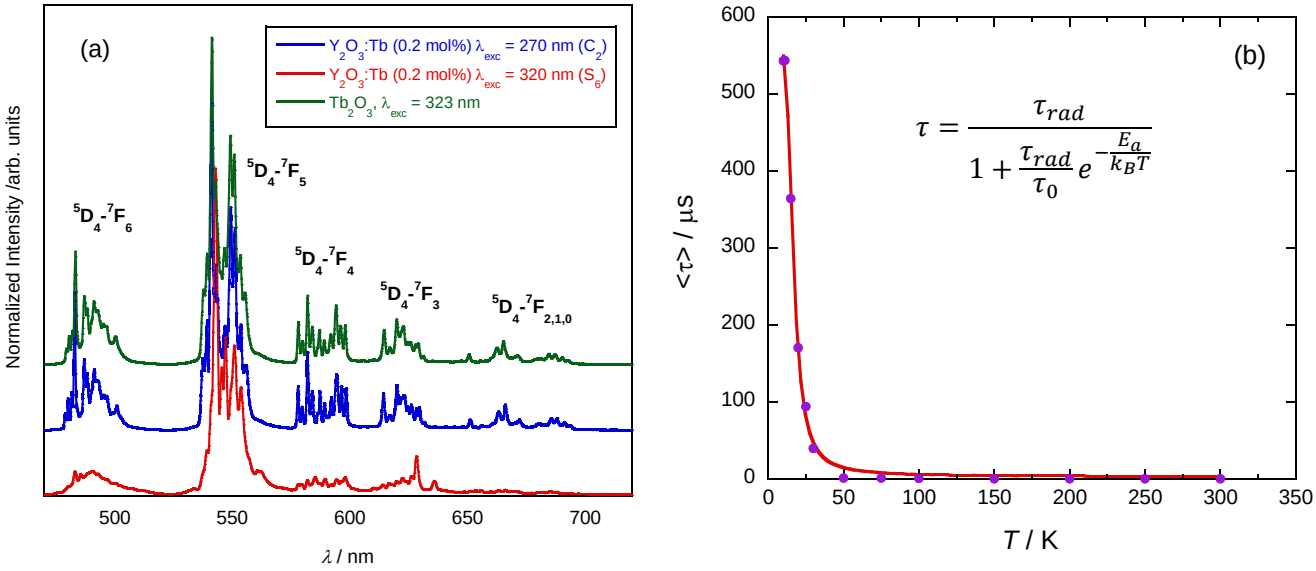

Fig. 6. (a) Emission spectra of Y_2O_3: 0.2mol% Tb^{3+} corresponding to the two non-equivalent crystallographic sites, C_2 and C_{3i}, compared with the one of Tb_2O_3 (b) Temperature dependence of the temporal evolution of the $^5D_4$ to $^7F_5$ Tb^{3+} luminescence of Tb_2O_3.

structure ($2E_g + 2A_{1g}$), although fewer modes are usually observed in the first case. As the number of observed Raman modes is increasing, we can infer that Tb_2O_3 is transiting from a C-type structure to a B-type structure. Above 12.2 GPa, the C-T_g mode has completely disappeared, together with the one at the highest frequency and the ones in the 140-380 cm^{-1} region, except one located at 210 cm^{-1}. Only 4 Raman modes are visible in the spectra in this pressure range.

This decrease in the number of Raman modes can be attributed to a second phase transition towards an A-type structure. No additional changes seem to happen up to the highest measured pressure, 21.5 GPa. This high-pressure behavior, with a C $\rightarrow$ B $\rightarrow$ A sequence is in agreement with the recently finds reported for this compound by XRD measurements. [33],[34]

The Grüneisen parameters (γ) were calculated for the cubic phase using eq.(7), where ω_{0i} is the frequency of the modes at ambient pressure and $\partial\omega_i/\partial P$ is their pressure dependence. B_0 =151.5 GPa is the bulk modulus. [20]

$$\gamma = \left(\frac{B_0}{\omega_{0\,i}}\right) \cdot \left(\frac{\partial \omega_i}{\partial P}\right) \qquad (7)$$

The obtained values are collected in Table 3. As it can be observed from the pressure derivatives and Grüneisen parameters, the first two Raman modes (93 and 105 cm^{-1}) do not shift with pressure, indicating that they might not be originated from the sample under study, although in other RE_2O_3, such as Eu_2O_3 or Sm_2O_3 and for Tb_2O_3 itself, Raman peaks at 94 cm^{-1} have been reported [20],[35] and the same behavior in the pressure derivatives has been observed among other C-type sesquioxides. [34]

Table 3. Symmetry, energy, pressure derivative and Grüneisen parameters γ of the Raman active modes of Tb_2O_3 corresponding to the cubic phase (0-7.5 GPa range).

Symmetry	ω_0/cm^{-1}	$\partial\omega/\partial P$ (cm^{-1}/GPa)	γ
T_g^1	93.0(1)	-0.14(2)	-0.22(3)
T_g^2	104.9(6)	0.01(1)	0.014(9)
A_g^1	117.1(1)	0.3(1)	0.4(1)
T_g^3	132.5(3)	0.5(2)	0.6(2)
E_g^1	143.2(2)	0.8(1)	0.8(1)
E_g^2	318.9(4)	3.2(1)	1.52(1)
T_g^5	365.9(2)	4.1(1)	1.69(4)
T_g^8	451.3(3)	5.1(1)	1.71(3)
T_g^9	576.0(3)	5.2(1)	1.36(3)

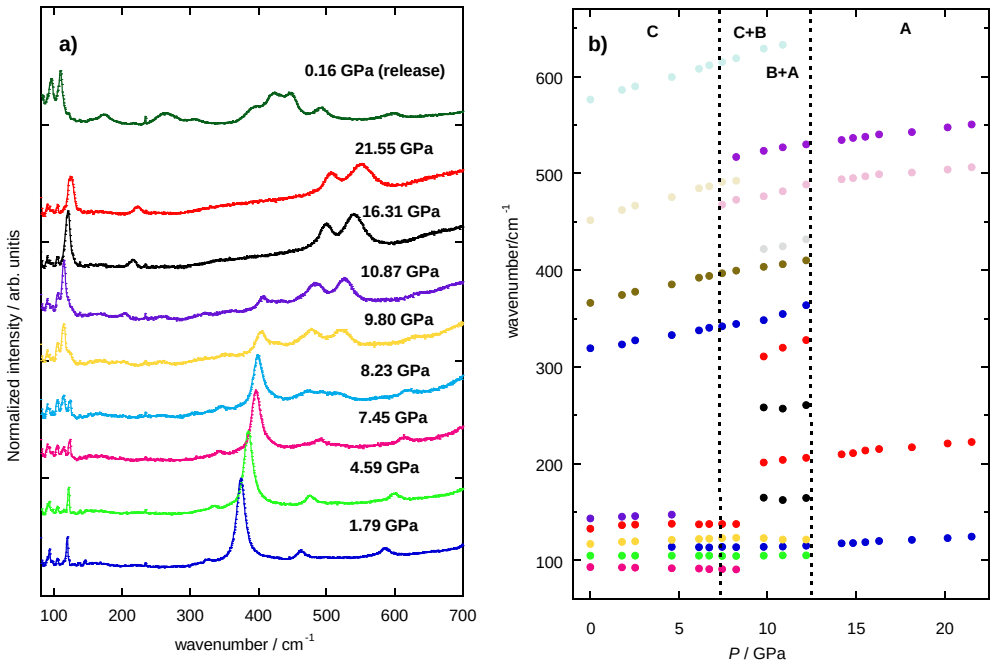

Fig. 7. RT Raman spectra of Tb_2O_3 upon increasing pressure (a) and shift of the Raman modes (b).

Upon releasing pressure, the Raman spectrum (Fig. 8) is different from the one at the highest measured pressure and different from the one of the starting material (Fig. 7), indicating an irreversible phase transition. Moreover, it is very similar to the monoclinic one reported for $SmGdO_3$ [36] or Gd_2O_3, [10] allowing us to infer that a structural phase transition A → B takes place.[34]

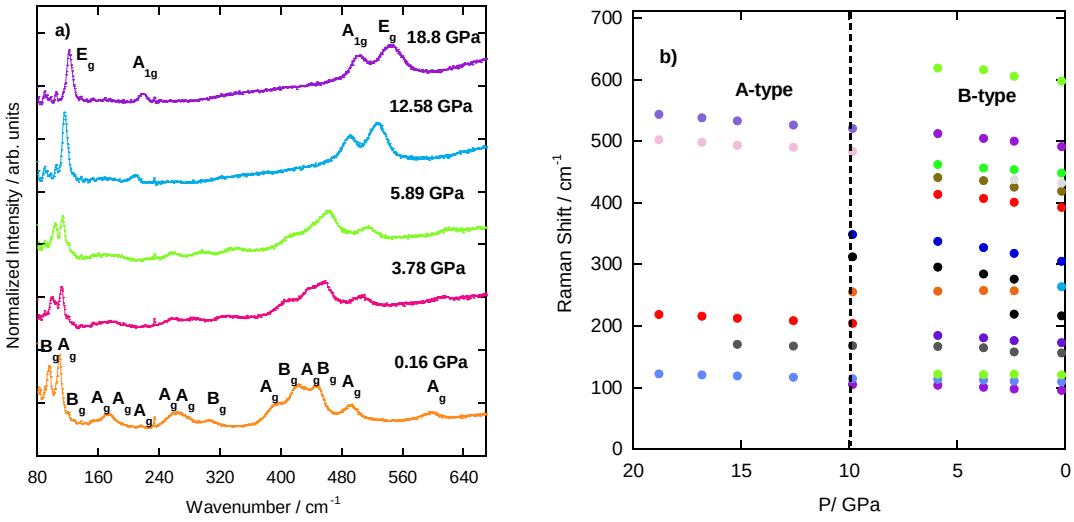

Fig. 8. Raman spectra of Tb_2O_3 upon releasing pressure (a) and energy shift of the Raman modes (b).

To further verify the transition sequence A → B upon releasing pressure, Raman data of A-type Sm_2O_3 (17.2 GPa) measured by S. Jiang *et al.*[37] has been compared with the Raman spectrum of Tb_2O_3 at 21.5 GPa (Fig 9 (a)). The XRD pattern of Sm_2O_3 at 13.5 GPa (taken also from ref. [37]) that corroborates the A-type phase is shown in Fig 9 (b). Moreover, B-type Eu_2O_3 has been synthesized by calcinating C-type Eu_2O_3 at 1400 ºC for 5h. The resultant Raman spectrum and XRD pattern are shown in Fig. 9 (c) and (d), respectively. The spectra of Tb_2O_3 at 21 GPa and after releasing pressure are quite similar to the ones of A-

type Sm_2O_3 and B-type Eu_2O_3, respectively, allowing us to confirm that an A $\rightarrow$ B transition takes place. Table 4 shows a comparison of the A-type and B-type Tb_2O_3 Raman wavenumbers with the Raman modes extrapolated for A-type Sm_2O_3 and the ones of B-type Eu_2O_3. B-type Tb_2O_3 Raman modes corresponds to the experimental ones after releasing pressure (0.16 GPa) while the modes of the A-type structure are extrapolated results. The Raman modes of B- and A-type Tb_2O_3 were assigned based on the very recently published experimental and theoretical study of this compound under compression by J. Ibáñez *et al*. [34], and whose frequencies are also compared in Table 4. Our experimental frequencies for B-type Tb_2O_3 are in accordance with those reported in the mentioned study (small differences could arise from the fact that our reported modes for this structure correspond to those before opening the DAC, at 0.16 GPa).

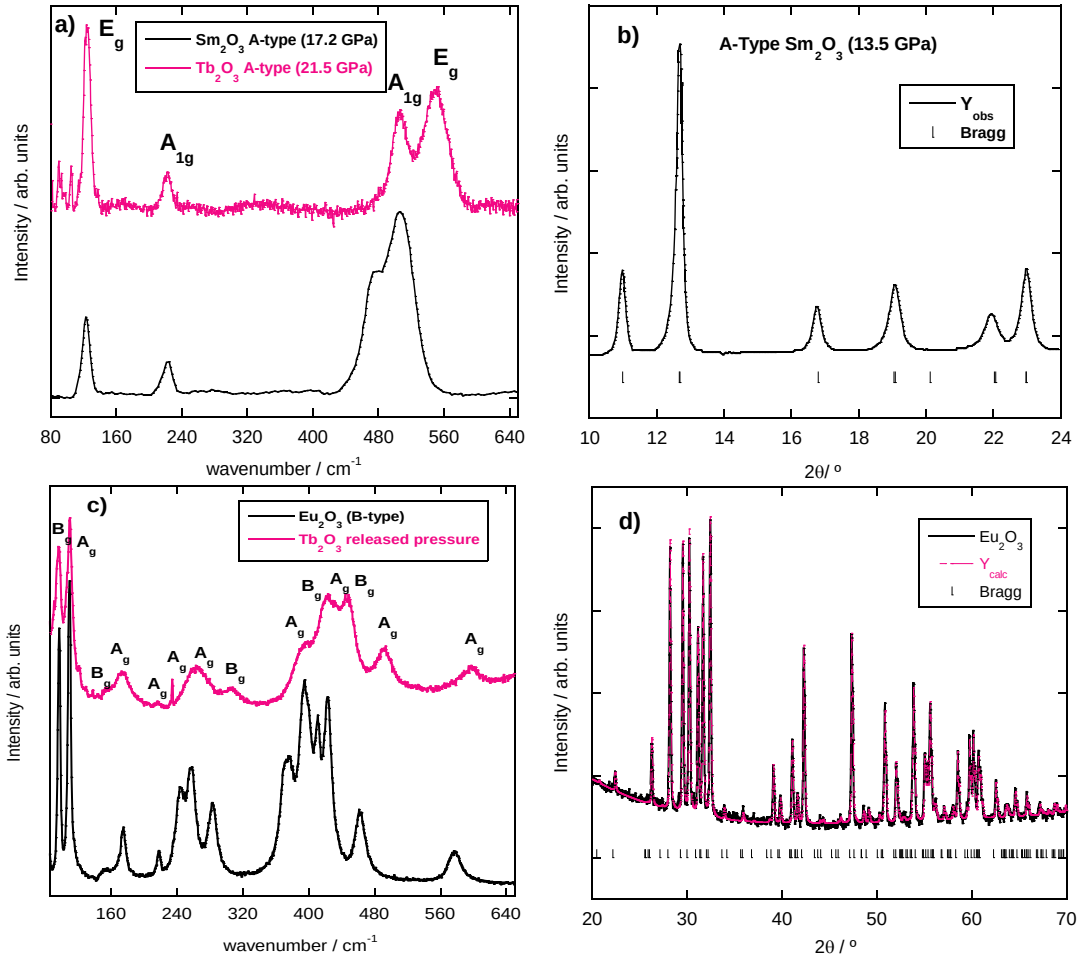

Fig. 9. Comparison between the Raman spectrum of A-type Sm_2O_3 (17.2 GPa) and the one of Tb_2O_3 measured at its highest pressure (a) and XRD pattern (λ= 0.6199 Å) of A-type Sm_2O_3 at 13. 5 GPa. Data of Sm_2O_3 was taken from ref [37] in both cases (b). Raman spectra of Tb_2O_3 upon pressure release compared with synthesized B-type Eu_2O_3 (c) and XRD pattern (λ=1.5418 Å) of as-synthesized B-type Eu_2O_3 (d).

Table 4. Comparison of A-type and B-type Tb_2O_3 Raman wavenumbers with the ones extrapolated for A-type Sm_2O_3 and B-type Eu_2O_3.

Modes (B-Type)	ω_0/cm^{-1} Eu_2O_3 [a]	ω_0/cm^{-1} Tb_2O_3 [a]	ω_0/cm^{-1} Tb_2O_3 [b]	Modes (A-Type)	ω_0/cm^{-1} Sm_2O_3 [c]	ω_0/cm^{-1} Tb_2O_3 [a]	ω_0/cm^{-1} Tb_2O_3 [b]
B_g	-	-	70.3	E_g	107.5(4)	104(1)	99
A_g	-	-	82.9	A_{1g}	197.7(9)	186(2)	183
B_g	96.23(4)	95.5(1)	96.8	A_{1g}	450.1(7)	471(1)	465
A_g	108.91(4)	109.2(1)	110.8	E_g	472.5(9)	505(1)	498
B_g	120(1)	121(1)	122.9				
A_g	154(1)	153.6(8)	156.3				
A_g	173.9(2)	173.1(4)	172.8				
A_g	217.4(2)	216(1)	216.5				
A_g	243.6(2)	-	261.8				
A_g	256.8(2)	263.9(4)	265.2				
B_g	282.9(2)	305.2(9)	306.6				
B_g	-	-	368.6				
A_g	373.3(2)	392.6(5)	391.7				
B_g	392.6(5)	419(1)	-				
A_g	410.7(2)	432(1)	426.2				
B_g	423.1 (1)	448.1(6)	446.0				
A_g	462.5(2)	491.3(4)	492.2				
A_g	577.3(3)	597.3(7)	596.7				

[a] This work, [b] Ref. [34], [c] Ref. [37]

In a similar way, the extrapolated wavenumbers for the Raman-active modes in the A-type structure are fairly similar to those reported by them, although ours are slightly higher. It is worth to point out that differences could also originate from the distinct transmitting media employed in the high-pressure Raman experiments: we use paraffin while they use a 4:1 methanol-ethanol mixture.

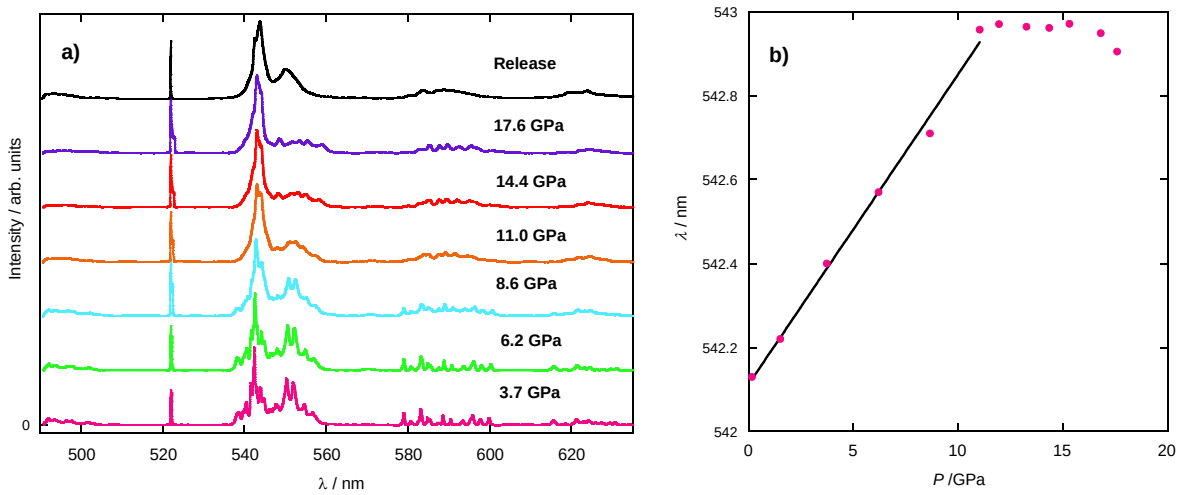

Fig. 10. PL spectra (λ_{exc} = 488 nm) of Tb_2O_3, including the $^5D_4$ - $^7F_5$ and $^5D_4$ - $^7F_4$ emission bands, upon increasing pressure. The resultant spectrum after releasing pressure is also shown (a). Pressure dependence of the wavelength for the most intense emission peak (b).

As previously mentioned, RE ions can be used as a structural probe, as some transitions have an intensity much more sensitive to changes in the local environment than normal *f-f* transitions.

These transitions, referred as *hypersentitive* transitions, generally obey the selection rules $\Delta J \leq 2$, $\Delta L \leq 2$ and sometimes $\Delta S = 0$. Probably the most well-known hypersensitive transition is the Eu^{3+} $^5D_0$-$^7F_2$ transition, although other RE have them as well. [38],[39] In the case of Tb^{3+} ions, the $^5D_4 - {}^7F_5$ transition is referred to as moderate sensitive to the environment.

For this reason, we have also used the RT Tb^{3+} high-pressure photoluminescence (PL) to study the structural implications in Tb_2O_3. Measurements were taken in the 490-650 nm range up to 17.5 GPa in a membrane DAC under a 488 nm excitation. Fig. 10 (a) shows selected photoluminescence spectra up to 17.5 GPa as well as the resulting spectra upon releasing pressure. At lower pressures, the spectra show the characteristic sharp line emission profiles of C-type Tb_2O_3, dominated by the $^5D_4$ - $^7F_5$ transition. With increasing pressure, the spectra shift toward longer wavelengths, being the pressure coefficient for the most intense peak at 542.1 nm ($^5D_4$ - $^7F_5$ transition), $\partial\lambda/\partial P$ = 0.07 nm/GPa (Figure 10 (b)). At 8.6 GPa there are appreciable changes in the intensities of the PL spectrum, mainly noticeable for intensity change of the $^5D_4$ - $^7F_5$ band, and with further increasing pressure some of the sharp emission lines that existed at RT have disappeared or cannot be completely resolved, probably due to the solidification of the pressure transiting media. Above 10 GPa, the peaks corresponding to the transitions $^5D_4$ - $^7F_6$ have completely disappeared and the ones corresponding to the transitions $^5D_4$ - $^7F_3$ have widened. All these variations point out a change in the crystallographic symmetry of Tb_2O_3 and hence, in the crystal environment of the Tb^{3+} ions, leading to differences in the PL spectra with respect to the one recorded at ambient conditions.

Upon decompression, the obtained PL spectrum is different from the one of the starting materials (Fig. 10 (a)), suggesting again an irreversible phase transition. The spectrum is very similar to the one obtained at the highest measured pressure, but with a less resolved emission profile, probably due to the similar symmetry in both cases and because of pressure effects.

We infer from the results of Raman measurements that the resulting changes in the emission profile are due to a C $\rightarrow$ B phase transition upon increasing pressure and a recover of the B phase when releasing that pressure. Photoluminescence measurements under compression allows us to distinguish only one phase transition, as the widening of the peaks with pressure can hinder the observation of subtle changes in the intensity of the emission peaks that could be related with the second phase transition (B $\rightarrow$ A).

4. Conclusions

In this work, we have characterized the C-Type Tb_2O_3 phase at ambient conditions, as well as its evolution in the low temperature and high-pressure regimes. No remarkable traces of Tb^{4+} were found in the sample. We have determined the pressure-induced phase transition sequence of Tb_2O_3 by following the changes in the emission spectra of Tb^{3+} and employing *in situ* Raman spectroscopy up to pressures of 18 GPa and 22 GPa, respectively. Raman results evidence a structural transition sequence C $\rightarrow$ B $\rightarrow$ A in the 0-22 GPa pressure range, in agreement with previous reports, [34] whereas only the first structural phase transition induces marked changes of the PL spectra. In any case, the monoclinic (B) phase is stable after total release of pressure. No evidence of structural phase transitions under temperature were observed spectroscopically. The anharmonic constant ratios in the model for Raman analysis suggest an optical phonon decay into two acoustic phonons, rather than three, in agreement with other isostructural RE sesquioxides. The excitation and emission spectra of Tb_2O_3 recorded at low temperature and at different emission and excitation wavelengths, suggest that only the emission from the non-centrosymmetric Tb^{3+}

crystallographic site (C_2) is observed. The reduction of Tb^{3+} lifetime upon increasing temperature have been modeled using an Arrhenius activation energy process. The fast decay, bright green emission and the good density makes Tb_2O_3 an interesting material for its use as a scintillator.

Declaration of competing interest

There are no conflicts to declare.

Acknowledgements

M.T Candela would like to thank University of Cantabria for her pre-doctoral grant, co-financed by the Government of Cantabria. Also, the authors acknowledge financial support from both, the European Research Council (ref NCLas H2020-EU829161) and the Spanish Ministerio de Economía Industria y Competitividad (PGC2018-101464-B-I00).

References

[1] M. Zinkevich, Thermodynamics of rare earth sesquioxides, Prog. Mater. Sci. 52 (2007) 597–647. https://doi.org/10.1016/j.pmatsci.2006.09.002.

[2] K.A. Irshad, N. V. Chandra Shekar, V. Srihari, K.K. Pandey, S. Kalavathi, High pressure structural phase transitions in Ho: Eu_2O_3, J. Alloys Compd. 725 (2017) 911–915. https://doi.org/10.1016/j.jallcom.2017.07.224.

[3] M.R. Levy, C.R. Stanek, A. Chroneos, R.W. Grimes, Defect chemistry of doped bixbyite oxides, Solid State Sci. 9 (2007) 588–593. https://doi.org/10.1016/j.solidstatesciences.2007.02.009.

[4] S. Ohmi, C. Kobayashi, I. Kashiwagi, C. Ohshima, H. Ishiwara, H. Iwai, Characterization of La_2O_3 and Yb_2O_3 thin films for high-k gate insulator application, J. Electrochem. Soc. 150 (2003) F134–F140. https://doi.org/10.1149/1.1581278.

[5] X.C. Zhang, J.M. Friedrich, M.A. Nearing, L.D. Norton, Potential use of rare earth oxides as tracers for soil erosion and aggregation studies, Soil Sci. Soc. Am.

J. 65 (2001) 1508–1515. https://doi.org/10.2136/sssaj2001.6551508x.

[6] G.H. S. Bär, H. Cheife, K. Petermann, Rare Earth Oxide Thin Films, Springer Berlin Heidelberg, 2007.

[7] Y. Zhang, I.H. Jung, Critical evaluation of thermodynamic properties of rare earth sesquioxides (RE = La, Ce, Pr, Nd, Pm, Sm, Eu, Gd, Tb, Dy, Ho, Er, Tm, Yb, Lu, Sc and Y), Calphad Comput. Coupling Phase Diagrams Thermochem. 58 (2017) 169–203. https://doi.org/10.1016/j.calphad.2017.07.001.

[8] Q. Guo, Y. Zhao, C. Jiang, W.L. Mao, Z. Wang, Phase transformation in Sm_2O_3 at high pressure: In situ synchrotron X-ray diffraction study and ab initio DFT calculation, Solid State Commun. 145 (2008) 250–254. https://doi.org/10.1016/j.ssc.2007.11.019.

[9] L. Wang, Y. Pan, Y. Ding, W. Yang, W.L. Mao, S. V. Sinogeikin, Y. Meng, G. Shen, H.K. Mao, High-pressure induced phase transitions of Y_2O_3 and Y_2O_3:Eu^{3+}, Appl. Phys. Lett. 94 (2009) 061921. https://doi.org/10.1063/1.3082082.

[10] F.X. Zhang, M. Lang, J.W. Wang, U. Becker, R.C. Ewing, Structural phase transitions of cubic Gd_2O_3 at high pressures, Phys. Rev. B - Condens. Matter Mater. Phys. 78 (2008) 064114. https://doi.org/10.1103/PhysRevB.78.064114.

[11] J. Sheng, B. Li-Gang, L. Jing, X. Wan-Sheng, L. Xiao-Dong, L. Yan-Chun, T. Ling-Yun, Z. Yu-Feng, Z. De-Chun, Z. Li-Rong, The phase transition of Eu_2O_3 under high pressures, Chinese Phys. Lett. 26 (2009) 076101. https://doi.org/10.1088/0256-307X/26/7/076101.

[12] X. Ren, X. Yan, Z. Yu, W. Li, K. Yang, X. Wang, Y. Liu, L. Wang, Size-dependent phase transition of Er_2O_3 under high pressure, Appl. Phys. Lett. 112 (2018) 143102. https://doi.org/10.1063/1.5017815.

[13] J. Yang, J. Gu, Hydrothermal Synthesis Y_2O_3:Yb^{3+}/Er^{3+} Nanospheres with Upconversion Luminescence from Green to Red, Nanosci. Nanometrology. 2 (2016) 41–45. https://doi.org/10.11648/j.nsnm.20160202.11.

[14] Y. Mao, T. Tran, X. Guo, J.Y. Huang, C.K. Shih, K.L. Wang, J.P. Chang, Luminescence of nanocrystalline erbium-doped yttria, Adv. Funct. Mater. 19 (2009) 748–754. https://doi.org/10.1002/adfm.200800880.

[15] G.J. Mccarthy, Crystal data on C- type terbium sesquioxide (Tb_2O_3), J. Appl. Cryst. 4 (1971) 399–400.

[16] B.M. Abu-Zied, A.R.N. Mohamed, A.M. Asiri, Effect of thermal treatment on the formation,textural and electrical conductivity properties of nanocrystalline Tb_4O_7, J. Nanosci. Nanotechnol. 15 (2015) 4487–4492. https://doi.org/10.1166/jnn.2015.9605.

[17] E. Zych, P.J. Dereń, W. Strek, A. Meijerink, W. Mielcarek, K. Domagala, Preparation, X-ray analysis and spectroscopic investigation of nanostructured Lu_2O_3:Tb, J. Alloys Compd. 323–324 (2001) 8–12. https://doi.org/10.1016/S0925-8388(01)01005-2.

[18] A. Diego-Rucabado, M.T. Candela, F. Aguado, J. González, F. Rodríguez, R.

Valiente, R. Martín-Rodríguez, I. Cano, A Comparative Study on Luminescence Properties of Y_2O_3: Pr^{3+} Nanocrystals Prepared by Different Synthesis Methods, Nanomaterials. 10 (2020) 1574. https://doi.org/10.3390/nano10081574.

[19] P. Veber, M. Velázquez, G. Gadret, D. Rytz, M. Peltz, R. Decourt, Flux growth at 1230 °c of cubic Tb_2O_3 single crystals and characterization of their optical and magnetic properties, CrystEngComm. 17 (2015) 492–497. https://doi.org/10.1039/c4ce02006e.

[20] J. Ibáñez, O. Blázquez, S. Hernández, B. Garrido, P. Rodríguez-Hernández, A. Muñoz, M. Velázquez, P. Veber, F.J. Manjón, Lattice dynamics study of cubic Tb_2O_3, J. Raman Spectrosc. 49 (2018) 2021–2027. https://doi.org/10.1002/jrs.5488.

[21] Y. Repelin, C. Proust, E. Husson, J.M. Beny, Vibrational spectroscopy of the C-form of yttrium sesquioxide, J. Solid State Chem. 118 (1995) 163–169. https://doi.org/10.1006/jssc.1995.1326.

[22] G. Schaack, J.A. Koningstein, Phonon and Electronic Raman Spectra of Cubic Rare-Earth Oxides and Isomorphous Yttrium Oxide*, J. Opt. Soc. Am. 60 (1970) 1110. https://doi.org/10.1364/josa.60.001110.

[23] M. Balkanski, R.F. Wallis, E. Haro, Anharmonic effects in light scattering due to optical phonons in silicon, Phys. Rev. B. 28 (1983) 1928–1934. https://doi.org/10.1103/PhysRevB.28.1928.

[24] I. Efthimiopoulos, S. Mayanna, E. Stavrou, A. Torode, Y. Wang, Extracting the Anharmonic Properties of the G-Band in Graphene Nanoplatelets, J. Phys. Chem. C. 124 (2020) 4835–4842. https://doi.org/10.1021/acs.jpcc.9b10875.

[25] S.D. Pandey, K. Samanta, J. Singh, N.D. Sharma, A.K. Bandyopadhyay, Raman scattering of rare earth sesquioxide Ho_2O_3: A pressure and temperature dependent study, J. Appl. Phys. 116 (2014) 133504. https://doi.org/10.1063/1.4896832.

[26] N. Bura, D. Yadav, J. Singh, N.D. Sharma, Phonon variations in nano-crystalline lutetium sesquioxide under the influence of varying temperature and pressure, J. Appl. Phys. 126 (2019) 245901. https://doi.org/10.1063/1.5125702.

[27] A. Taube, A. Łapińska, J. Judek, M. Zdrojek, Temperature dependence of Raman shifts in layered $ReSe_2$ and $SnSe_2$ semiconductor nanosheets, Appl. Phys. Lett. 107 (2015) 013105. https://doi.org/10.1063/1.4926508.

[28] F. Benz, H.P. Strunk, J. Schaab, U. Künecke, P. Wellmann, Tuning the emission colour by manipulating terbium-terbium interactions: Terbium doped aluminum nitride as an example system, J. Appl. Phys. 114 (2013) 073518. https://doi.org/10.1063/1.4818815.

[29] P. Dorenbos, The $4f^n \leftrightarrow 4f^{n-1}$ 5d transitions of the trivalent lanthanides in halogenides and chalcogenides, J. Lumin. 91 (2000) 91–106. https://doi.org/10.1016/S0022-2313(00)00197-6.

[30] D. Avram, B. Cojocaru, M. Florea, C. Tiseanu, Advances in luminescence of lanthanide doped Y_2O_3: case of S_6 sites, Opt. Mater. Express. 6 (2016) 1635. https://doi.org/10.1364/ome.6.001635.

[31] D. den Engelsen, P.G. Harris, T.G. Ireland, G. Fern, J. Silver, Symmetry-Related Transitions in the Photoluminescence and Cathodoluminescence Spectra of Nanosized Cubic $Y_2O_3:Tb^{3+}$, ECS J. Solid State Sci. Technol. 4 (2015) R145–R152. https://doi.org/10.1149/2.0011512jss.

[32] D. Den Engelsen, J. Silver, T.G. Ireland, G.R. Fern, P.G. Harris, Photoluminescence study of symmetry-related transitions in the spectrum of $Y_2O_3:Tb^{3+}$, Proc. Int. Disp. Work. (2015) 528–531.

[33] F.J. Manjón, J. Angel, S. Tresserras, J. Ibáñez, A.L.J. Pereira, Pressure-Induced Phase Transitions in Sesquioxides, Crystals. 9 (2019) 630. https://doi.org/10.3390/cryst9120630.

[34] J. Ibáñez, J.Á. Sans, V. Cuenca-Gotor, R. Oliva, Ó. Gomis, P. Rodríguez-Hernández, A. Muñoz, U. Rodríguez-Mendoza, M. Velázquez, P. Veber, C. Popescu, F.J. Manjón, Structural and Lattice-Dynamical Properties of Tb_2O_3 under Compression: A Comparative Study with Rare Earth and Related Sesquioxides, Inorg. Chem. 59 (2020) 9648–9666. https://doi.org/10.1021/acs.inorgchem.0c00834.

[35] M. V. Abrashev, N.D. Todorov, J. Geshev, Raman spectra of R_2O_3 (R - Rare earth) sesquioxides with C-type bixbyite crystal structure: A comparative study, J. Appl. Phys. 116 (2014) 103508. https://doi.org/10.1063/1.4894775.

[36] Y. Sharma, S. Sahoo, A.K. Mishra, P. Misra, S.P. Pavunny, A. Dwivedi, S.M. Sharma, R.S. Katiyar, Structural phase transition of ternary dielectric $SmGdO_3$: Evidence from angle dispersive x-ray diffraction and Raman spectroscopic studies, J. Appl. Phys. 117 (2015) 094101. https://doi.org/10.1063/1.4913776.

[37] S. Jiang, J. Liu, C. Lin, X. Li, Y. Li, High-pressure x-ray diffraction and Raman spectroscopy of phase transitions in Sm_2O_3, J. Appl. Phys. 113 (2013) 113502. https://doi.org/10.1063/1.4795504.

[38] C.K. Jorgensen, B.R. Judd, Hypersensitive pseudoquadrupole transitions in lanthanides, Mol. Phys. An Int. J. Interface Between Chem. Phys. 8 (1964) 281–290. https://doi.org/10.1080/00268977700103141.

[39] G. Ligner, R. Mohan, S. Knittel, G. Duportail, Hypersensitivity of terbium and europium ions luminescence in biological substrates, Spectrochim. Acta Part A Mol. Spectrosc. 46 (1990) 797–802. https://doi.org/10.1016/0584-8539(90)80037-Y.

Graphical Abstract (for review)

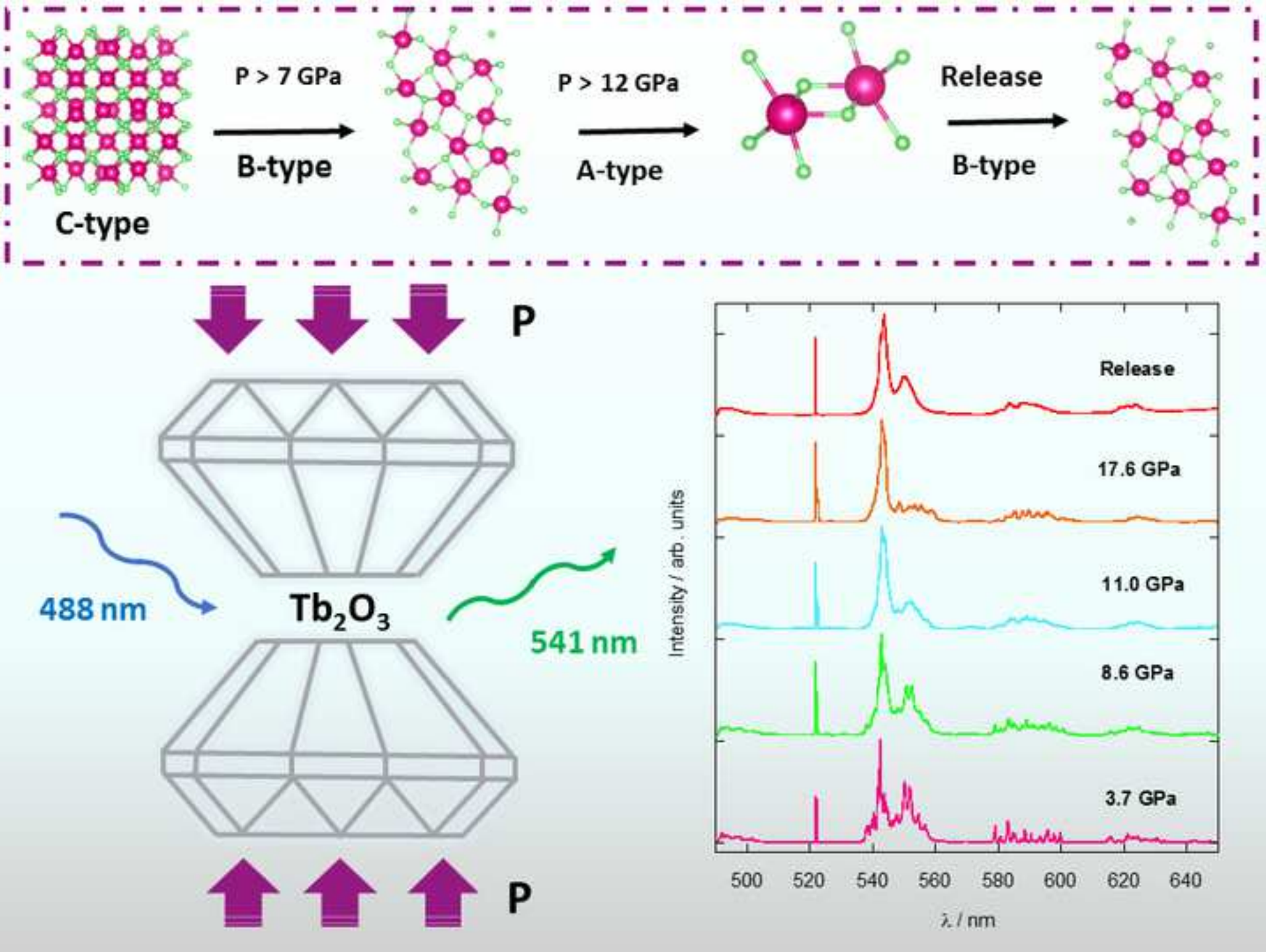

Highlights

1) Tb_2O_3 shows two high-pressure structural phase transitions with symmetry change, which involve variations in spectroscopic features.
2) Monoclinic phase is stable upon pressure release (metastability).
3) Tb_2O_3 shows potential characteristics for scintillation purposes.
4) Raman and luminescent are efficient probes for symmetry changes in sexquioxides.

CRediT author statement

M. T. Candela: Investigation, Writing - original draft

F. Aguado: Conceptualization, Supervision, Writing - review & editing

J. González-Lavín: Investigation

J. A. González: Investigation, Writing - review & editing

R. Valiente: Conceptualization, Supervision, Writing - review & editing, Funding acquisition

*Declaration of Interest Statement

Declaration of interests

☒ The authors declare that they have no known competing financial interests or personal relationships that could have appeared to influence the work reported in this paper.

☐The authors declare the following financial interests/personal relationships which may be considered as potential competing interests: